Microporous and Mesoporous Materials 316 (2021) 110947

Contents lists available at ScienceDirect

Microporous and Mesoporous Materials

journal homepage: http://www.elsevier.com/locate/micromeso

Doubling CO_2/N_2 separation performance of CuBTC by incorporation of 1-*n*-ethyl-3-methylimidazolium diethyl phosphate

Muhammad Zeeshan [a,b], Hasan Can Gulbalkan [a], Zeynep Pinar Haslak [a], Seda Keskin [a,b,**], Alper Uzun [a,b,c,*]

[a] Department of Chemical and Biological Engineering, Koç University, Rumelifeneri Yolu, Sariyer, Istanbul, 34450, Turkey
[b] Koç University TÜPRAŞ Energy Center (KUTEM), Koç University, Rumelifeneri Yolu, Sariyer, Istanbul, 34450, Turkey
[c] Koç University Surface Science and Technology Center (KUYTAM), Koç University, Rumelifeneri Yolu, Sariyer, Istanbul, 34450, Turkey

ARTICLE INFO

Keywords:
Metal organic frameworks (MOFs)
Ionic liquids (ILs)
Composite materials
CO_2 separation

ABSTRACT

1-ethyl-3-methylimidazolium diethyl phosphate ([EMIM][DEP]) was incorporated into copper benzene-1,3,5-tricarboxylate, CuBTC. Consequences of molecular interactions on the CO_2 separation performance of CuBTC were investigated. Scanning electron microscopy and X-ray diffraction results showed that the surface morphology and crystal structure of CuBTC remained intact upon the incorporation of the ionic liquid (IL); and the results of thermogravimetric analysis and infrared spectroscopy indicated the presence of interactions between the anion of the IL and the open metal sites of CuBTC. Gas adsorption measurements for the pristine CuBTC and IL-incorporated CuBTC were performed at 25 °C in a pressure range of 0.1–1 bar. Data showed that ideal CO_2/CH_4 and CO_2/N_2 selectivities of IL-incorporated CuBTC were 1.6- and 2.4-times higher compared to those of the pristine CuBTC at 0.01 bar, respectively. Moreover, for the CO_2/CH_4:50/50 and CO_2/N_2:15/85 mixtures, the corresponding selectivities were improved by more than 1.5- and 1.9-times compared to that of pristine CuBTC at 0.01 bar, respectively.

1. Introduction

CO_2 separation from flue gas and natural gas streams helps in reducing the excess CO_2 emissions to the atmosphere and in upgrading the total calorific value, respectively. Developing economical processes that can selectively capture CO_2 from these gas streams with improved separation efficiency is highly desirable. Compared to the existing technologies for CO_2 capture and separation processes, such as amine-based absorption and membrane-based gas separation processes, adsorption-based gas separation offers advantages of being energy efficient along with lower operating cost requirements [1–3]. Numerous porous materials, such as zeolites, activated carbons, graphene aerogels, carbon nanotubes, alumina, and metal organic frameworks (MOFs) have been widely explored for the adsorption-based gas separation processes [4–12]. Among these materials, MOFs are of great interest for gas adsorption and separation owing to their large surface areas, high pore volumes, and good chemical and thermal stabilities [13]. These are porous crystalline materials offering tunability in the structure because of the ability to alter the metal nodes and linkers to adjust their pore sizes and shapes [14]. Although pristine MOFs offer high gas adsorption capacities, numerous studies demonstrated that adsorption capacity and separation performance of a pristine MOF can be improved by various post-synthesis modification techniques [15]. Among these approaches, incorporation of ionic liquids (ILs) into MOFs has drawn significant attention. ILs are salts that are composed of cations and anions with tunable physicochemical properties because of the presence of an almost unlimited number of anion and cation combinations [16,17]. Thus, incorporation of ILs into MOFs offers a broad potential and flexibility in modifying adsorption capacities and separation performance of MOFs.

To date, a number of studies demonstrated that combining ILs with MOFs introduced new preferential adsorption sites for the guest molecules, leading to significant improvements in gas adsorption capacities and separation performances [18–24]. For instance, in one of the earlier reports, 1-*n*-butyl-3-methylimidazolium tetrafluoroborate ([BMIM][BF_4]) was incorporated into CuBTC [19]. The data demonstrated that upon the incorporation of IL, the ideal CH_4/CO_2 and CH_4/N_2

* Corresponding author. Department of Chemical and Biological Engineering, Koç University, Rumelifeneri Yolu, Sariyer, Istanbul, 34450, Turkey.
** Corresponding author. Department of Chemical and Biological Engineering, Koç University, Rumelifeneri Yolu, 34450, Sariyer, Istanbul, Turkey.
E-mail addresses: skeskin@ku.edu.tr (S. Keskin), auzun@ku.edu.tr (A. Uzun).

https://doi.org/10.1016/j.micromeso.2021.110947
Received 3 November 2020; Received in revised form 28 January 2021; Accepted 29 January 2021
Available online 5 February 2021
1387-1811/© 2021 The Authors. Published by Elsevier Inc. This is an open access article under the CC BY-NC-ND license (http://creativecommons.org/licenses/by-nc-nd/4.0/).

selectivities of CuBTC improved by 1.5-times. This pioneering study was then followed by several other studies focusing on different IL-MOF pairs [25–29]. All these studies highlight that incorporation of ILs into MOFs has a potential to improve the gas separation performance. However, the current knowledge on the structure-performance relationships on these novel composites is still limited, and there exists an almost limitless number of structural possibilities. One way to overcome this difficulty is to investigate the consequences of systematic structural changes in the individual components of the composites on the corresponding gas separation performance. Focusing on a single type of MOF and investigating as many different IL structures as possible can offer a promise. In this regard, CuBTC is a good candidate, as it is one of the few commercially available MOFs with a high gas adsorption capacity and there already exists a good number of reports covering various IL/CuBTC composites [11,19,23,30].

For instance, we incorporated 1-*n*-butyl-3-methylimidazolium hexafluorophosphate ([BMIM][PF_6]) and 1-*n*-butyl-2,3-dimethylimidazolium hexafluorophosphate ([BMMIM][PF_6]) into CuBTC to investigate the influence of methylation of the imidazolium ring at the C2 position on gas separation performance of IL-incorporated CuBTC [30]. Results showed improvements in CO_2/N_2 and CH_4/N_2 selectivities of IL-incorporated CuBTC compared to parent CuBTC at low pressure. Furthermore, data also indicated that when a non-methylated IL ([BMIM][PF_6]) was incorporated into CuBTC, the resulting IL/CuBTC composite shows a better gas separation performance compared to IL/CuBTC composite with a methylated IL ([BMMIM][PF_6]). We also incorporated seven different $[BMIM]^+$-based ILs in CuBTC and showed that ν(Cu–O) bond becomes weaker in IL/CuBTC composites as a result of the interactions between the IL molecules and the open metal sites of CuBTC, controlling the uptake capacity and thermal stability limits of IL-incorporated CuBTC samples [31]. Moreover, the degree of weakening in ν(Cu–O) bond can be tuned by the interionic interaction energy between the cation and the anion of the IL probed by the ν(C2H) infrared (IR) band position of the bulk IL. Similarly, Mohamedali et al. [32] incorporated 1-*n*-butyl-3-methylimidazolium acetate ([BMIM][OAc]) and 1-*n*-propyl-3-methylimidazolium bis(trifluoro-methylsulfonyl) imide [PMIM][Tf_2N] into the pores of CuBTC. Their results demonstrated that [BMIM][OAc]-incorporated CuBTC exhibited a higher CO_2 adsorption capacity at a low pressure compared to that of the pristine CuBTC, whereas incorporation of the [PMIM][Tf_2N] into CuBTC did not improve the CO_2 adsorption capacity of the parent MOF. On the basis of these results, it can be concluded that upon the incorporation of IL with a small anion ($[OAc]^-$) into CuBTC, CO_2 adsorption capacity increased, whereas upon the incorporation of the IL with a relatively large anion ($[Tf_2N]^-$) into CuBTC showed no improvement in the uptake capacity of the composite sample.

These structural factors were further investigated computationally. Vicent-Luna et al. [33] performed molecular simulations to analyze the change in CO_2, CH_4, and N_2 adsorption of CuBTC upon the incorporation of ILs having the same 1-ethyl-3-methylimidazolium ($[EMIM]^+$) cation with five different anions into CuBTC pores. Results showed that IL/CuBTC composites are promising materials for CO_2/CH_4 and CO_2/N_2 separations compared to pristine CuBTC especially at low pressures. Moreover, our group investigated seven imidazolium based IL-incorporated CuBTC composites using grand canonical Monte Carlo (GCMC) simulations to predict CO_2/CH_4, CO_2/N_2, and CH_4/N_2 separation performance of the composites [23]. Results exhibited that IL/CuBTC composites have higher CO_2/CH_4 and CO_2/N_2 selectivities compared to the parent MOF.

As summarized above, there are several studies focusing on the IL/CuBTC composites, making CuBTC an excellent platform for investigating the structure-performance relationships in IL/MOF composites. Thus, it is crucial to consider different ILs to gain more insights into these relationships. Here, we aimed at extending the list of investigations reported on IL-incorporated CuBTC materials to contribute to the knowledge on the structural factors controlling the interactions between the IL and MOF and the consequences of these interactions on the corresponding gas adsorption and separation performance. In this regard, 1-ethyl-3-methylimidazolium diethyl phosphate ([EMIM][DEP]) was incorporated into CuBTC. [EMIM][DEP] was chosen based on the conclusion from a recent report presenting the structural factors controlling the thermal stability limits of IL/MOF composites [34]. The data indicated that the decomposition temperature of [EMIM][DEP]/-CuBTC composite was higher than that of bulk IL, an opposite behavior compared to the case with the most of the other IL/CuBTC composites. This difference in decomposition mechanism was attributed to the differences in the interactions between the IL and CuBTC. Besides, [EMIM][DEP] has an excellent affinity and solubility towards CO_2 compared to CH_4 and N_2 [35,36].

Hence, [EMIM][DEP]/CuBTC composite was prepared by post-synthetic modification of CuBTC via wet-impregnation method and then characterized in detail combining the strengths of various techniques to identify the structural changes upon the incorporation of IL into the CuBTC and to reveal the molecular interactions responsible for these changes. Finally, to assess the consequences of the IL-MOF interactions on the gas uptakes, adsorption of CO_2, CH_4, and N_2 gases were measured in pristine CuBTC and [EMIM][DEP]/CuBTC composite. Results showed that upon incorporation of IL into CuBTC, CO_2/CH_4 and CO_2/N_2 selectivities of IL-incorporated CuBTC composites were improved compared to those of the parent MOF. Results presented here extend the knowledge on the structural factors controlling the gas separation performance of IL/CuBTC composites and provide additional insights into the structure-performance relationships in these materials, much needed towards the design of materials with high CO_2 separation performance.

2. Materials and methods

2.1. Materials

[EMIM][DEP], CuBTC (Basolite C300), and analytical grade acetone were acquired from Sigma-Aldrich. Each chemical was kept in an Argon-filled Labconco glovebox. CO_2 (99.9 vol%), CH_4 (99.95 vol%), and N_2 (99.9 vol%) were purchased from Air Liquide.

2.2. Sample preparation

[EMIM][DEP]/CuBTC composite with 30 wt% stoichiometric IL loading was prepared via wet-impregnation method. First, 20 mL of acetone was mixed with 0.3 g of IL in a beaker and the resulting solution was stirred for 1 h under ambient temperature and pressure conditions to get a homogeneous solution. Subsequently, 0.7 g of pristine CuBTC activated overnight under vacuum at 105 °C was added to the IL-acetone solution. The resulting mixture was stirred for approximately 6 h in an open atmosphere at 35 °C to allow slow evaporation of the solvent. After the complete evaporation of acetone from the mixture, the resulting sample was further dried overnight in a furnace at 105 °C to obtain IL-incorporated CuBTC composite.

2.3. X-ray fluorescence (XRF) spectroscopy

To conduct XRF measurements, a Bruker S8 Tiger spectrometer using an X-ray tube with a Rh anode under Helium atmosphere was utilized.

2.4. Brunauer-emmett-teller (BET) analysis

The BET analyses of pristine CuBTC and IL-incorporated CuBTC were performed on a Micromeritics ASAP 2020 surface area and porosimetry system. Prior to measurements, pristine CuBTC and IL-incorporated CuBTC were degassed under vacuum at 125 °C for approximately 12 h. N_2 gas adsorption-desorption isotherm for pristine CuBTC and IL/CuBTC composite were obtained at −196 °C. The N_2 isotherm data were

fitted to BET equation in a relative pressure range of 0.05–0.65 to calculate the surface area, whereas *t*-plot method was employed to calculate the pore volume of the samples.

2.5. Scanning electron microscopy (SEM)

A Zeiss Evo LS 15 electron microscope was utilized to obtain the surface morphologies of each sample. SEM images of the samples were obtained at a magnification of 500 k× and 1 k× under ultra-high vacuum with an accelerating voltage of 3 kV.

2.6. X-ray diffraction (XRD) spectroscopy

XRD measurements were conducted on a Bruker D8 Advance instrument with Cu-Kα1 radiation source (λ = 1.5418 Å). Each XRD pattern was obtained using a step size of 0.0204° in a 2θ range of 5–50°.

2.7. Thermal gravimetric analysis (TGA)

A TA Instruments Q500 thermogravimetric analyzer was used to perform thermal analysis of pristine CuBTC, [EMIM][DEP], and IL/CuBTC composite. Each measurement was performed in an inert atmosphere using N_2 as purge and balance gas at 60 and 40 mL/min, respectively. For each measurement, approximately 0.15 g of the sample was loaded onto a pan, and then the sample was heated from room temperature to 120 °C at a heating rate of 5 °C/min. At 120 °C, the temperature was kept isothermal for 8 h. Afterwards, at a heating rate of 2 °C/min, temperature of the samples was raised to 700 °C. The derivative onset (T'_{onset}) temperatures considered in this study were obtained by the extrapolation of the derivative thermogravimetry (TG) curves.

2.8. Infrared spectroscopy (IR)

A Thermo Scientific Nicolet iS50 in transmission mode was utilized to record the IR spectra of pristine CuBTC, bulk IL, and IL/CuBTC composite. Sixty four scans were acquired for background measurement, whereas 512 scans were collected for sample measurements. The IR spectrum for each sample was obtained at a resolution of 2 cm^{-1} within a spectral range of 4000 to 400 cm^{-1}. Voigt function was employed in Fityk to perform the deconvolutions of peaks [37].

2.9. Nuclear magnetic resonance (NMR)

^{13}C NMR of bulk [EMIM][DEP] was obtained using a Bruker Avance Neo 500 MHz NMR spectrometer. Deuterated solvent ($CDCl_3$) used in NMR analysis was purchased from Sigma-Aldrich.

2.10. Quadrupole time-of-flight mass spectrometry (Q-TOF-MS)

Q-TOF-MS measurement on bulk [EMIM][DEP] was performed using a Waters Vion IMS Q-TOF-MS.

2.11. X-ray photoelectron spectroscopy (XPS) analysis

XPS measurements for pristine CuBTC and [EMIM][DEP]/CuBTC composite were performed on a Thermo Scientific K-Alpha spectrometer with an aluminum anode (Al Kα = 1468.3 eV). The spectra of the samples were recorded using Avantage 5.9 software.

2.12. Gas adsorption measurements

A Micromeritics (Particulate Systems) High Pressure Volumetric Analyzer HPVA II-200 was utilized to measure CH_4, CO_2, and N_2 adsorption isotherms of pristine CuBTC and [EMIM][DEP]/CuBTC composite. 0.4 g of the sample was used for each measurement. First, each sample was degassed for approximately 12 h under vacuum at 125 °C in the degas port. Before starting the analysis of the samples, the sample holder was purged with He in the analysis port. Then, CH_4, CO_2, and N_2 gas adsorption isotherms were obtained at 25 °C in a pressure range of 0.1–1 bar. Each adsorption isotherm was fitted to Langmuir-Freundlich model by utilizing Ideal Adsorbed Solution Theory $(IAST)^{++}$ software [38]. The corresponding fitting parameters were summarized in the Supporting Information (SI) as Table S1.

2.13. Computational methodology

To perform the Grand Canonical Monte Carlo (GCMC) simulations, first [EMIM][DEP] structure was optimized by density functional theory (DFT) calculations as described below and [EMIM][DEP]/CuBTC composite was minimized as described in our previous work [23]. GCMC simulations were conducted using the RASPA simulation code version 2.0.37 [39]. The potential parameters for van der Waals interactions for both the IL and MOF atoms were obtained from the Dreiding force field [40]. CO_2 and CH_4 were modeled as three-site and single-site rigid molecules with 12-6 Lennard Jones potential [41,42]. N_2 was modeled as a three-site rigid molecule with N atoms at the two sites and the third site was the center of mass with partial point charges [43]. IL loading was set to 13 IL molecule per unit cell of a MOF, which corresponds to 26.2 wt%. Partial charges were reassigned to MOF and IL atoms after IL incorporation using the charge equilibration (Qeq) method [44]. GCMC simulations were carried out for 50 000 cycles with the first 5000 cycles for initialization and the last 45 000 cycles for taking ensemble averages. GCMC simulations for single component CO_2, CH_4, and N_2 were performed between 0.1 and 1 bar at 298 K. The isosteric heats of adsorption (Q_{st}) for gas molecules were computed at 1 bar from GCMC simulations.

The quantitative investigation of the CO_2, CH_4, and N_2 interactions with [EMIM][DEP] was carried by performing DFT calculations. All possible conformations of the molecules were located by using Becke-three-parameter-Lee-Yang-Parr (B3LYP) functional including Grimme's D2 correction and all electron 6-31G* basis set using Gaussian09 program package [45–47]. The vibrational frequency analysis was implemented to ensure no imaginary frequency remained on the optimized geometries and to ensure the global minimum geometries were obtained. Binding energies between the gases and the IL molecule and natural bond orbital (NBO) atomic charges were further calculated with 6–311++G** basis set by performing single point calculations on the optimized geometries. The binding energies between the adsorbed gases and the IL were calculated by using the equation:

$$\Delta E_{bind} = E_{A+B} - E_A - E_B$$

where E_{A+B} is the energy of the system consisting the adsorbed gas molecule (CO_2, CH_4, or N_2) and the adsorbent (IL), E_A is the energy of the adsorbent, and E_B is the energy of the gas molecule.

Conductor-like Screening Model for Realistic Solvents (COSMO-RS) calculations were performed using COSMOthermX(C30_160) software as described previously [48–51]. TZVP parameterizations was employed to compute the solubility of CH_4, CO_2, and N_2 in the bulk [EMIM][DEP]. The COSMOthermX software calculates the pure compound solubility of a gas with partial pressure P_j in a given solvent using an iterative procedure. For each compound j the mole fraction x_j is varied until the partial pressure of the compound is equal to the given reference pressure P. The P_i is calculated as:

$$P_j = P_j^o x_j \gamma_j$$

P_j^o represents pure compound vapor pressure, x_j is mole fractions of the gas in liquid, and γ_j is the activity coefficients. Finally, the gas solubilities in ILs were calculated by considering the system as a ternary mixture of cation, anion, and gas [48–51].

3. Results and discussions

The purity of bulk [EMIM][DEP] was confirmed by Q-TOF-MS and ^{13}C NMR measurements as presented in Fig. S1 and Fig. S2 given in the Supporting Information, SI, respectively. XRF analysis was performed on the as-prepared [EMIM][DEP]/CuBTC to determine the elemental composition of each element in the composite. Based on the elemental compositions presented in Table 1, the corresponding IL loading in the composite was determined as approximately 25 wt%. This loading amount was previously reported as the highest IL loading that can be achieved for IL-incorporated MOFs before exceeding the wetness point [19].

Surface area and pore volume of the parent CuBTC and the [EMIM][DEP]/CuBTC composite were determined from N_2 physical adsorption isotherms as presented in Fig. 1. Results demonstrated that pristine CuBTC and its composite with the IL present typical type-I N_2 adsorption isotherms, a characteristic feature of microporous materials. Thus, we inferred that CuBTC maintains its microporosity upon the incorporation of IL.

Data further showed that the pristine CuBTC has a BET surface area and pore volume of 1324 $m^2\ g^{-1}$ and 0.52 $cm^3\ g^{-1}$, respectively, whereas the corresponding values for [EMIM][DEP]/CuBTC composite were found to be 131 $m^2\ g^{-1}$ and 0.06 $cm^3\ g^{-1}$, respectively. These notable decreases indicate that the MOF's pores were mostly occupied by the IL molecules, confirming the successful incorporation of IL into CuBTC consistent with previous reports [19,30,31]. However, we also note that N_2 uptake of the IL/MOF composite depends on the N_2 solubility in the corresponding IL at the measurement conditions of −196 °C. Thus, the IL molecules located near the pore openings might be blocking the N_2 diffusion to the partially filled pores; thus, we emphasize that the BET results may not be very reliable for the IL/MOF composites [29,31,52]. To further confirm the successful incorporation of IL, we washed the composite samples with benzyl alcohol, which is sufficiently large (8.0 Å) that cannot enter the pore openings (3.4 Å) of CuBTC [53,54]. The IR spectra of the composite before and after washing, the filtrate, and those of pristine CuBTC and IL are presented in Fig. S3 in the SI. Accordingly, the IR spectrum of the filtrate lacks any features associated with the IL, whereas the spectra of the washed and dried sample still preserve the features related with the IL. Thus, we confirm that IL molecules were mostly present inside the cages of CuBTC in the composite.

The surface morphologies of pristine CuBTC and [EMIM][DEP]/CuBTC composite were characterized by SEM as illustrated in Fig. 2. The SEM images of IL/CuBTC composite indicate the regular octahedral morphology, consistent with the previously reported surface morphology of pristine CuBTC [19,55]. Hence, we inferred that upon the incorporation of IL, CuBTC mostly preserved its morphology.

XRD patterns presented in Fig. 3 showed that incorporation of IL did not affect the crystalline structure of CuBTC as the peak positions of the individual features were mostly preserved, except for minor changes in the peak intensities. Intensities of the XRD peaks are sensitive to the presence of chemical species or bulky molecules inside the MOF's pores [56,57]. Thus, we infer that these slight changes observed in the intensities of some of the peaks are possibly associated with the changes in electronic environment of the CuBTC as a result of the presence of IL molecules inside the pores of CuBTC.

Table 1
Cu and P amount in the [EMIM][DEP]/CuBTC composite determined by XRF measurement. The IL structure is presented in the footnote.*

Formula	Concentration (wt %)
CHO	79.7
Cu	17.8
P	2.2

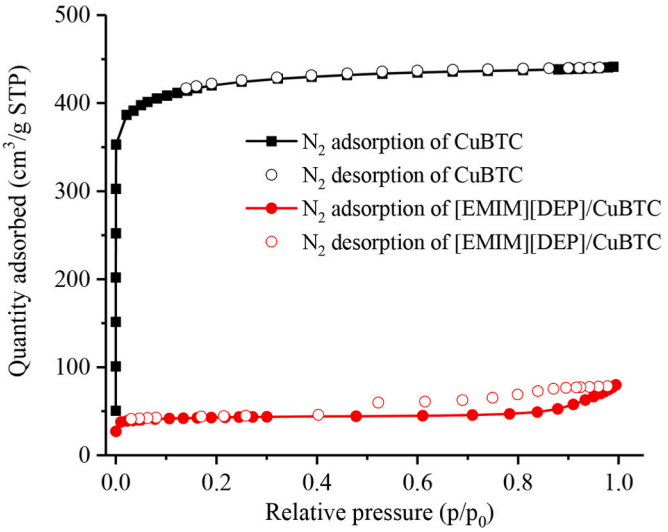

Fig. 1. N_2 physical adsorption-desorption isotherms of pristine CuBTC and [EMIM][DEP]/CuBTC composite at −196 °C.

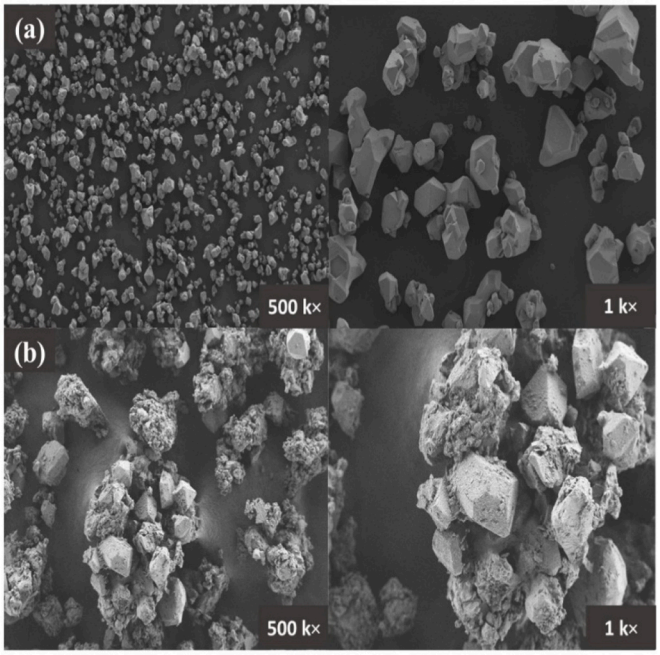

Fig. 2. Surface morphology images of (a) CuBTC and (b) [EMIM][DEP]/CuBTC obtained at magnifications of 500 k× and 1 k×.

Thermal stabilities of the pristine CuBTC and its [EMIM][DEP]/CuBTC composite were retrieved from our recent study reporting the structural factors controlling the thermal stability limits of IL/MOF composites [34]. These results were examined to understand the influence of changes in the electronic environment on the decomposition temperature of composite material. Fig. 4 compares TGA results of pristine CuBTC, bulk [EMIM][DEP], and [EMIM][DEP]/CuBTC composite.

The initial weight loss of the samples up to 150 °C in the TGA curves presented in Fig. 4 can be attributed to the removal of the physisorbed moisture content. Accordingly, pristine CuBTC and the bulk [EMIM][DEP] decompose through a typical one-step decomposition mechanism with the corresponding T'_{onset} values of 324 and 185 °C, respectively, whereas the [EMIM][DEP]/CuBTC composite showed a T'_{onset} of 224 °C presenting a two-step decomposition mechanism. Here, we note that IL/

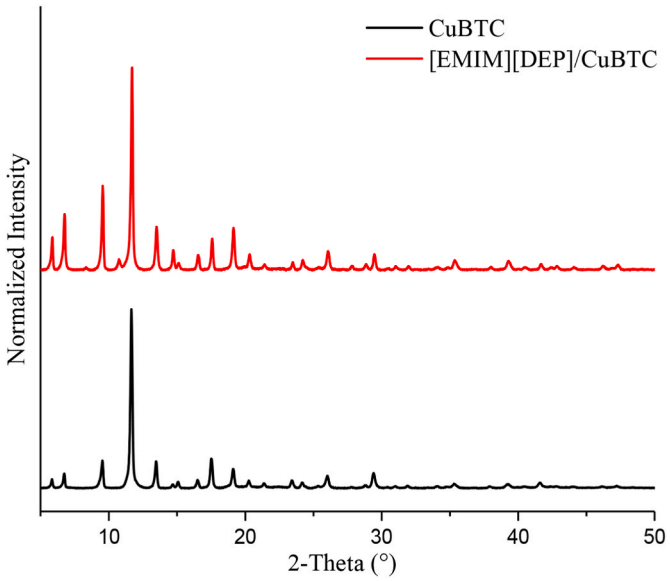

Fig. 3. Powder XRD patterns of pristine CuBTC and [EMIM][DEP]/CuBTC composite.

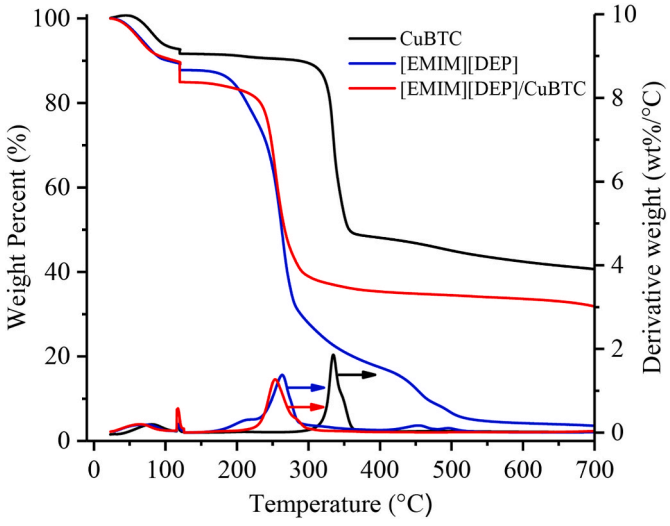

Fig. 4. TGA and DTG curves of pristine CuBTC, bulk [EMIM][DEP], and [EMIM][DEP]/CuBTC composite. Modified and reprinted with permission from Ref. [34] Copyright 2019 American Chemical Society.

MOF composite has a higher T'_{onset} compared to the decomposition temperature of the bulk IL. This change in T'_{onset} can be ascribed to the existence of direct IL-MOF interactions in the composite material offering a completely different behavior of the IL when it is confined, consistent with the previous reports [34]. IR spectra of the parent CuBTC, bulk [EMIM][DEP], and [EMIM][DEP]/CuBTC composite were acquired to further elucidate these interactions. The corresponding IR spectra in the regions of 2800–3200 cm^{-1} and 400–1800 cm^{-1} are presented in Fig. 5.

Fig. 5 shows that characteristic peaks of the bulk [EMIM][DEP] were still present in the spectra of IL-incorporated CuBTC, further confirming the successful incorporation of IL into CuBTC. To analyze the FTIR result, we first deconvoluted the IR peaks into individual contributors. Fig. S4 in the SI demonstrates an example of peak fitting process of pristine CuBTC, bulk IL, and IL/CuBTC composite in the IR region of 540–400 cm^{-1}. The major peaks in the IR spectrum of [EMIM][DEP] at 1042, 1228, and 1570 cm^{-1} were assigned to imidazole ring δ(C–H),

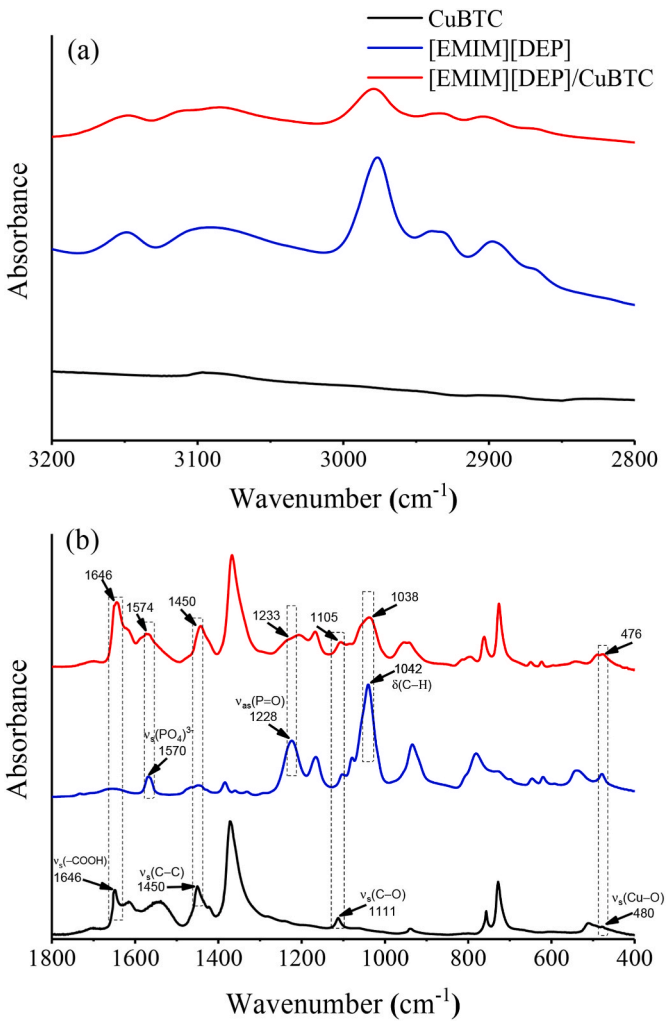

Fig. 5. IR spectra of CuBTC, bulk [EMIM][DEP], and [EMIM][DEP]/CuBTC composite: (a) 3200–2800 cm^{-1} and (b) 1800–400 cm^{-1}.

ν_{as}(P═O), and $\nu_s(PO_4)^{3-}$ group, respectively [58–60]. The δ(C–H) of imidazole ring red-shifted to 1038 cm^{-1}, whereas ν_{as}(P═O) and $\nu_s(PO_4)^{3-}$ bands demonstrated a blue-shift of 5 and 4 cm^{-1}, respectively, in the IR spectra of the IL/CuBTC composite. Moreover, the band at 3071 cm^{-1} corresponding to ν(C2H) band of the bulk IL blue-shifted to 3080 cm^{-1}. Such strong blue-shift observed in ν(C2H) band position of the bulk IL indicates the weakening of interactions between the IL's cation and anion upon the successful incorporation into the pores of CuBTC. On the other hand, IR spectrum of pristine CuBTC also showed peaks at 480, 1111, 1450, and 1646 cm^{-1} corresponding to ν_s(Cu–O), ν_s(C–O) ν_s(C–C), and ν_s(—COOH) bands, respectively [31,61]. Upon the incorporation of IL into CuBTC, both ν_s(Cu–O) and ν_s(C–C) bands presented red-shifts of 4 and 6 cm^{-1}, respectively, whereas no shifts were observed for ν_s(C–O) and ν_s(—COOH) modes. The red-shift in ν_s(Cu–O) band of CuBTC illustrated that the electronic environment inside the MOF cage was significantly influenced by the presence of IL, leading to a weakening in the Cu–O bond. These changes in the positions of the IR bands of bulk IL and pristine CuBTC imply the possibility that anion of the IL is sharing its electrons with the open metal sites of CuBTC, confirming the existence of direct interactions between IL and MOF in the composite material.

To further investigate the interactions between CuBTC and IL in the composite sample, we obtained the XP spectra of pristine CuBTC and [EMIM][DEP]/CuBTC composite as presented in Fig. 6. The characteristics peaks related to CuBTC, such as Cu $2p_{2/3}$, Cu $2p_{1/2}$, C 1s, and O 1s,

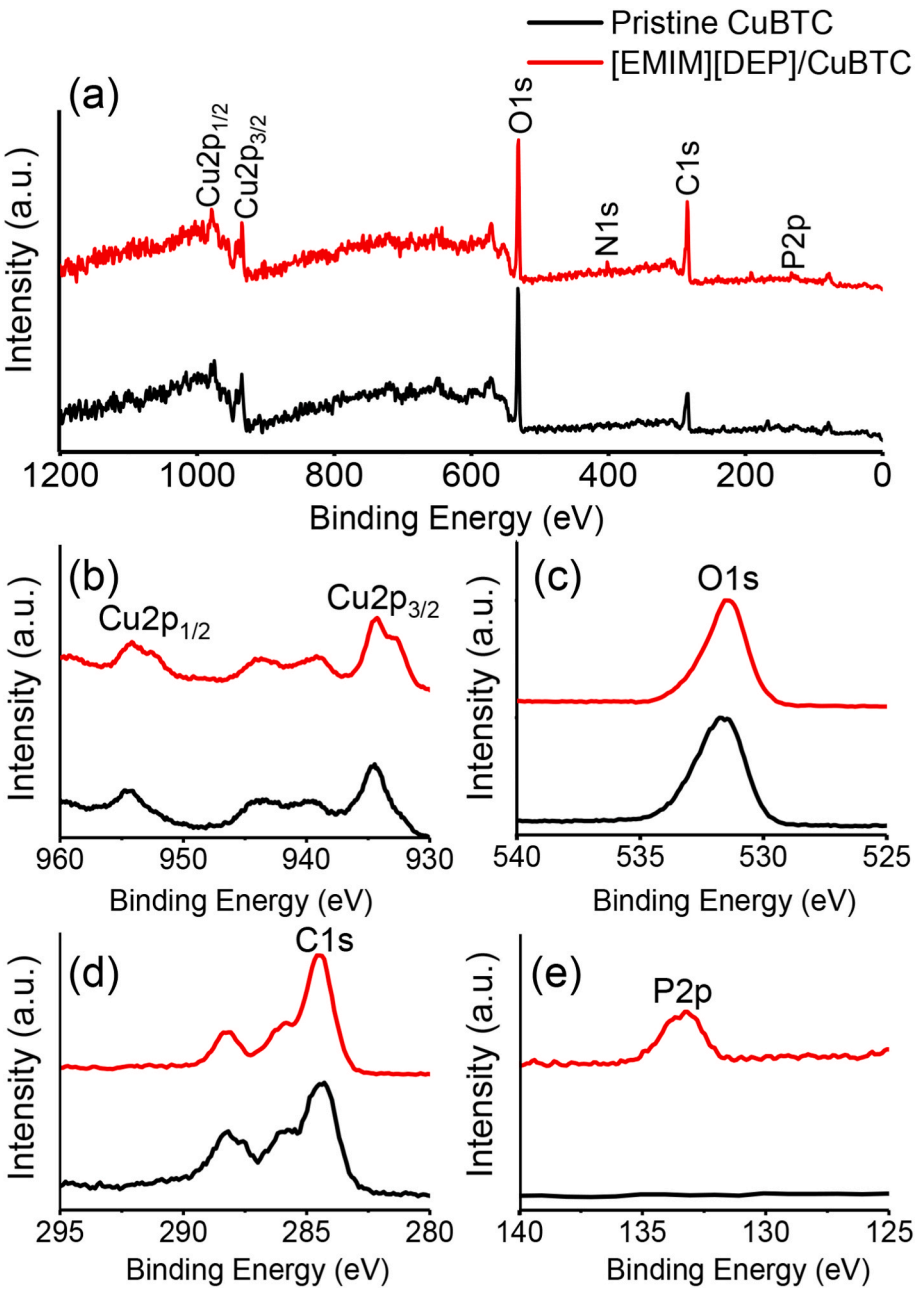

Fig. 6. XPS spectra of (a) survey spectra, (b) Cu 2p, (c) O 1s, (d) C 1s, and (e) P 2p regions of pristine CuBTC and [EMIM][DEP]/CuBTC composite.

were observed in XP spectra of pristine CuBTC [62,63]. Whereas, as expected, a P 2p peak associated with the anion $[DEP]^-$ of IL was present in XP spectra of [EMIM][DEP]/CuBTC composite. Furthermore, the Cu $2p_{2/3}$ peak at 934.5 eV in pristine CuBTC showed a red shift of 0.2 eV upon the incorporation of IL into CuBTC. This slight shift in the binding energy indicates a change in the electron density around the Cu atom due the interactions between open metal sites and anion part of IL. This observation is also consistent with the FTIR results, where a red shift was observed in the ν_s(Cu–O) band of CuBTC upon the incorporation of IL. This red shift was attributed to the weaking of ν_s(Cu–O) band in the IL/CuBTC composite due to possible interaction of Cu atoms with IL molecules, consistent with earlier interpretation [31].

To elucidate the impact of these direct interactions on the gas adsorption and separation performance of [EMIM][DEP]-incorporated CuBTC, volumetric gas adsorption measurements of CO_2, CH_4, and N_2 for pristine CuBTC and [EMIM][DEP]/CuBTC composite were obtained up to 1 bar at 25 °C as presented in Fig. 7(a–c). Data presented in Fig. 7 (a–c) illustrate that upon the incorporation of IL into CuBTC, the uptake capacity of each gas in [EMIM][DEP]/CuBTC decreased compared to that of pristine CuBTC. These decreases in the adsorption capacity of the IL-incorporated CuBTC is expected because the accessible surface area and pore volume for the guest adsorbate were reduced upon the incorporation of IL into CuBTC pores. However, it is noted that extends of these decreases on the adsorption capacities were different for each gas. This difference can be attributed to distinct affinities of each gas towards the formation of new adsorption sites upon incorporation of IL. Result shown in Fig. S5 in the SI demonstrate that adsorption capacities of CH_4 and N_2 decreased considerably (to 23% and 16% of their values in pristine CuBTC, respectively) more in the composite compared to corresponding decrease in CO_2 uptake (37%) at a low pressure, which could be ascribed to the great affinity of CO_2 towards the phosphate-based anion of the IL. Consistently, Indarto et al. [64] investigated the interactions of CO_2 with ILs having phosphorous-based anions in detail using molecular simulations, and reported that phosphate-based anion

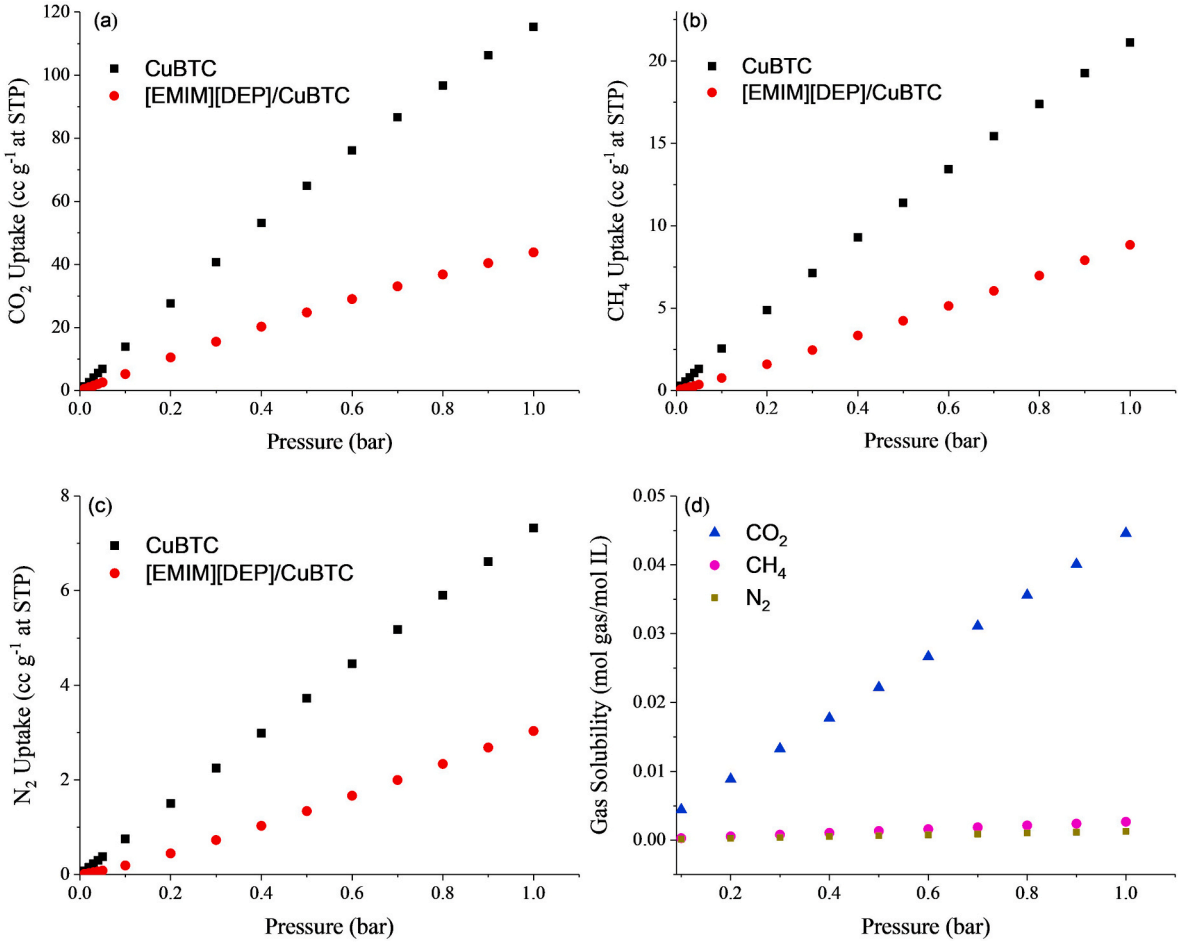

Fig. 7. Single component adsorption isotherms of (a) CO_2; (b) CH_4; and (c) N_2 for pristine CuBTC and [EMIM][DEP]/CuBTC at 25 °C; (d) solubility of N_2, CH_4, and CO_2 in bulk [EMIM][DEP] computed by COSMO-RS calculations at 25 °C. Data are provided in cc gas per gram of composite.

plays a significant role in the effective CO_2 absorption due to the CO_2-phlicity.

Furthermore, we also performed GCMC simulations to investigate CO_2, CH_4, and N_2 adsorption in the [EMIM][DEP]/CuBTC composite. The comparison between experimental and simulated (scaled as presented previously [23]) gas uptakes for CO_2, CH_4, and N_2 are presented in Fig. S6 in the SI in a pressure range of 0.1–1 bar at 298 K. GCMC simulations using the Dreiding force field overestimated all gas uptakes except CO_2 uptakes after 0.8 bar. Overestimation of gas uptakes may be attributed to the perfect crystal assumption used in simulations. Thus, we used the scaling factors defined in our previous work and obtained a better agreement between experiments and simulations [23].

Furthermore, solubility of N_2, CH_4, and CO_2 gases in the bulk [EMIM][DEP] as shown in Fig. 7 (d) was qualitatively estimated by the COSMO-RS calculations performed at 25 °C in a pressure range of 0.1–1 bar. CO_2 has more than one-order-of-magnitude higher solubility compared to CH_4, and a two-order-of-magnitude higher solubility compared to N_2, in agreement with our adsorption measurements. Furthermore, we also performed DFT calculations to investigate the CO_2, CH_4, and N_2 interactions with bulk [EMIM][DEP] to complement the COSMO-RS results. First, the most stable conformer was determined by considering several different cation-anion pair configurations representing [EMIM][DEP]. Three of these conformer geometries with the lowest equilibrium energies are illustrated in Fig. S7 in the SI. The data indicated that the equilibrium energy of the optimized geometry obtained on the Conformer 1 was found to be 0.25 kJ/mol lower than that of Conformer 2 and it was 6.59 kJ/mol lower than that of Conformer 3, in which the non-bonded pairs on oxygen atoms of the anion form intermolecular hydrogen bonds with the cation. Thus, we conducted the rest of the investigation on the interactions of guest gas molecules with [EMIM][DEP] using the Conformer 1. The optimization of [EMIM][DEP] with CO_2, CH_4, and N_2 molecules showed that three of the gases interact differently with the IL molecules as presented in Fig. S8 in the SI. CO_2 makes very close contact with both anion and cation of the IL; one of the oxygen atoms forms two hydrogen bonds with cation's hydrogens on the ethyl substituent (at 2.47 and 2.74 Å), while positively charged central C atom ($q_C = 1.026e$) is attracted by the negatively charged O atom of the anion ($q_O = -1.175e$) with a C–O distance of 2.64 Å. Hydrogen atoms of CH_4 molecule make hydrogen bonds with two oxygen atoms of the anion, while one of nitrogen atoms of N_2 forms hydrogen bonds with the hydrogen atoms on the imidazolium ring (at 2.67 and 2.68 Å). CO_2 shows the highest affinity towards [EMIM][DEP] with the calculated binding energy of 32.9 kJ/mol due to the stabilizing interactions formed between the gas and the IL, whereas CH_4 and N_2 have lower affinities towards the IL molecules with calculated binding energies of 15.6 and 13.2 kJ/mol, respectively. This difference in the affinity of the IL towards these guest molecules is strongly consistent with the results of COSMO-RS calculations. Thus, the lower CH_4 and N_2 adsorption capacities of [EMIM][DEP]/CuBTC composite can be associated with the presence of weak interactions and poor solubility of CH_4 and N_2 in the corresponding IL. Changes of various levels in the uptakes of different gases imply that gas separation performance of [EMIM][DEP]-incorporated CuBTC would change. Hence, to assess the separation performance of the materials, ideal CO_2/CH_4 and CO_2/N_2 selectivities, and their mixture counterparts were calculated for CuBTC and [EMIM][DEP]/CuBTC composite. Adsorption isotherms of CO_2, CH_4,

and N_2 were fitted to Langmuir-Freundlich model to calculate the ideal selectivities and the Ideal Adsorption Solution Theory (IAST) was employed to estimate CO_2/CH_4:50/50 and CO_2/N_2:15/85 mixture selectivities [65].

The corresponding ideal and mixture selectivities of the samples are presented in Fig. 8. Data showed that the ideal CO_2/CH_4 selectivity of pristine CuBTC improved from 4.6 to 7.4 corresponding to an increase of 1.6-times (Fig. 8 c) upon the incorporation of IL into CuBTC at 0.01 bar. More interestingly, at 0.01 bar, ideal CO_2/N_2 selectivity of [EMIM][DEP]/CuBTC was higher (42.3) compared to that of pristine CuBTC (17.6), corresponding to an increase of approximately 2.4-times upon the IL incorporation (Fig. 8 d). It was reported that in the low pressure range, gas uptakes are significantly influenced by the affinity of adsorbent surface towards the guest molecules [25,26]. Since CO_2 interacts much more strongly with the phosphate-based anion of the IL compared to CH_4 and N_2 do, as evident from the results of COSMO-RS and DFT calculations, the presence of [EMIM][DEP] inside the MOF cages favors the selective adsorption of CO_2 molecules compared to CH_4 and N_2. As a result, CO_2/CH_4 and CO_2/N_2 selectivities of IL/CuBTC composite improved significantly especially at low pressures. . However, at high pressures, the overall gas uptake depends more on the available pore volume rather than the competitive adsorption of guest molecules. Therefore, ideal CO_2/CH_4 and CO_2/N_2 selectivities decrease as the pressure increases. Moreover, at a comparatively higher pressure (>0.7 bar), CO_2 separation performance of IL/CuBTC composite is lower than that of the pristine CuBTC. This result can be attributed to the presence of less space available for guest molecules because of the presence of IL molecules inside the pores of MOF. In addition, we obtained the isosteric heats of adsorption (Q_{st}) values from GCMC simulations. Results showed that Q_{st} values for CO_2, CH_4, and N_2 were 27.50, 20.42, and 16.86 kJ/mol in [EMIM][DEP]/CuBTC composite, which are higher compared to the Q_{st} values (21.82, 16.86, and 13.46 kJ/mol) of the corresponding gases in pristine CuBTC, respectively. These results indicate that CO_2 has a higher adsorption energy compared to those of CH_4 and N_2. The difference between the adsorption energies of these gasses becomes more significant in the presence of IL, which leads to an enhancement in the CO_2 selectivities in the composite.

IAST calculations were done to predict the corresponding CO_2/CH_4:50/50 and CO_2/N_2:15/85 mixture selectivities of pristine CuBTC and [EMIM][DEP]/CuBTC composite. At 0.01 bar, CO_2/CH_4:50/50 selectivity of CuBTC improved from 4.4 to 6.6, whereas CO_2/N_2:15/85 separation performance improved from 16.2 to 31.1 upon the incorporation of IL into CuBTC. Moreover, the normalized CO_2/CH_4:50/50 and CO_2/N_2:15/85 selectivities showed 1.5- and 1.9-times improvements in [EMIM][DEP]-incorporated CuBTC. These improvements in gas separation performance suggest that [EMIM][DEP]/CuBTC has a strong potential for CO_2 separation applications.

To further illustrate the influence of different IL-CuBTC combinations on the gas separation performance of IL-incorporated CuBTC, we compared the gas separation performance of [EMIM][DEP]/CuBTC with those of the previously reported IL-incorporated CuBTC composites. The comparison presented in Fig. 9 shows the normalized ideal CO_2/CH_4 and CO_2/N_2 selectivities of various IL/CuBTC composites prepared by the incorporation of approximately 25–30 wt% IL loading. Normalized selectivities were obtained by dividing the CO_2/CH_4 and CO_2/N_2 selectivities of the composite samples to the corresponding values of a parent CuBTC at a similar pressure point. Thus, a normalized value greater than unity indicates an improvement in the gas separation performance of the

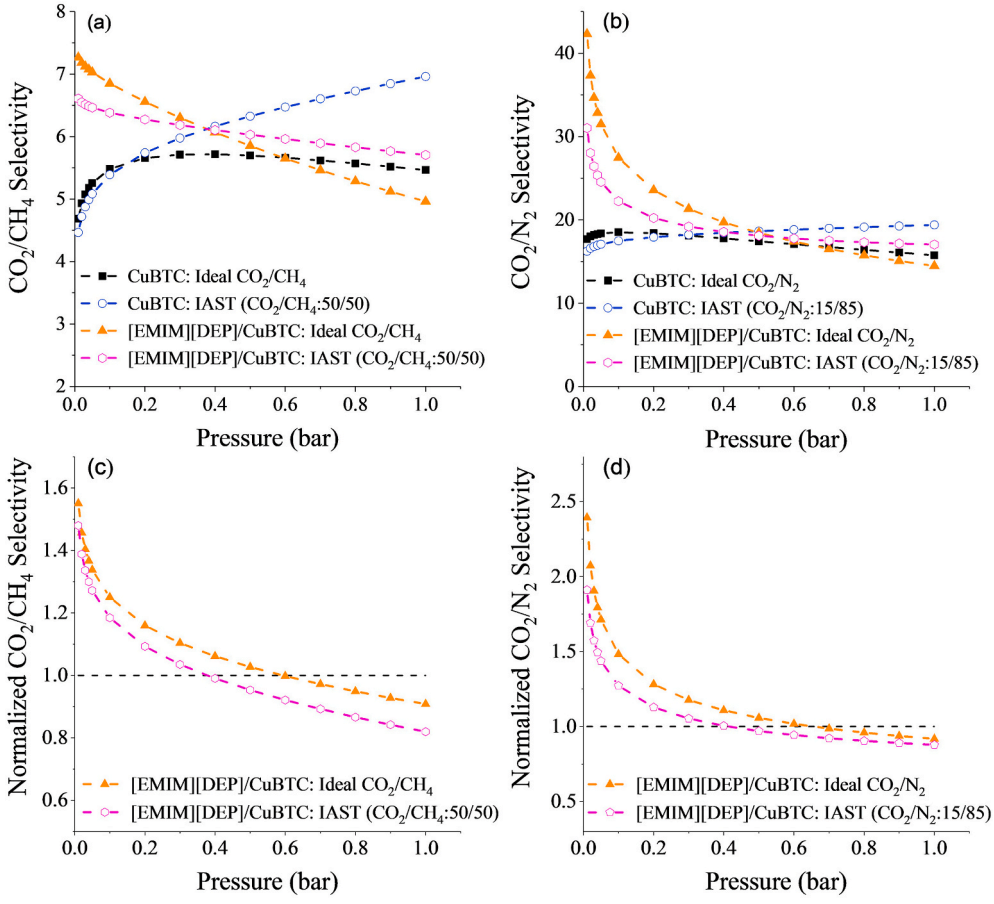

Fig. 8. (a) CO_2/CH_4 and (b) CO_2/N_2 selectivities of pristine CuBTC and [EMIM][DEP]/CuBTC composite, (c) CO_2/CH_4 and (d) CO_2/N_2 normalized selectivities of the [EMIM][DEP]/CuBTC composite.

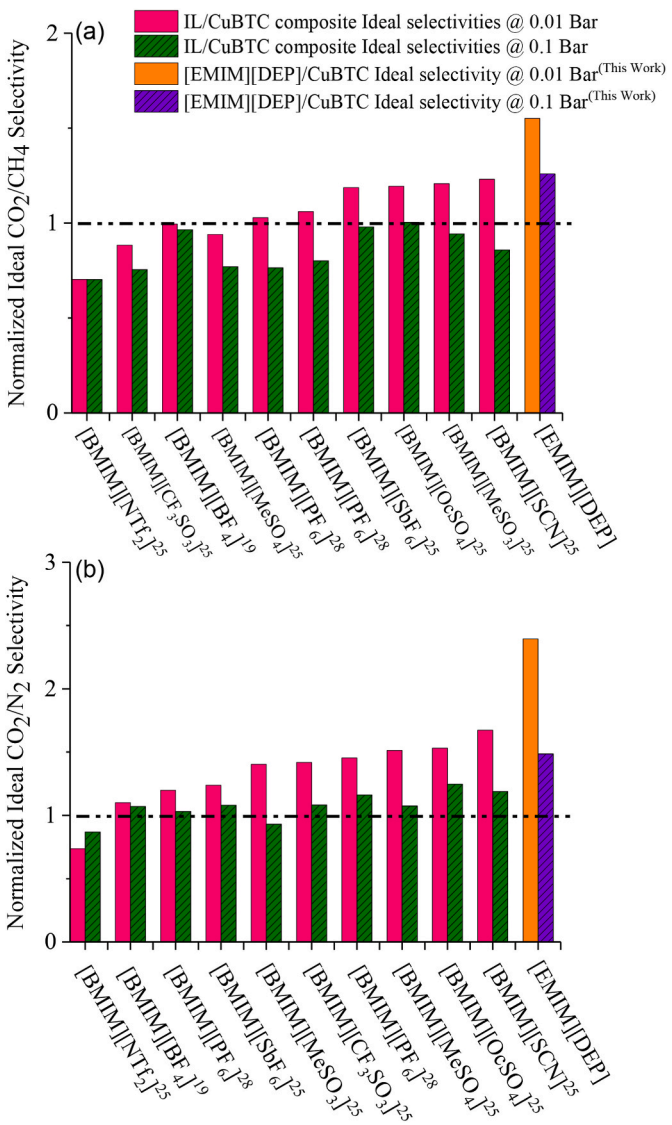

Fig. 9. Normalized ideal (a) CO_2/CH_4 and (b) CO_2/N_2 selectivities of IL-incorporated CuBTC samples at 0.01 and 0.1 bar. Ideal CO_2/CH_4 and CO_2/N_2 selectivities of pristine CuBTC are 4.6 and 17.6, respectively, at 0.01 bar and 5.4 and 19.8, respectively, at 0.1 bar.

parent MOF upon the incorporation of IL. Here, we note that the data presented in Fig. 9 demonstrate the gas separation performance of the IL/CuBTC composites at only low pressures as the effect of IL on the gas uptakes becomes more significant at these pressures compared to the case at high pressures. Accordingly, when both IL and CuBTC have a similar hydrophilic character, the gas separation performance of the composite is generally improved. On the other hand, when IL and CuBTC have opposite hydrophilicities, gas separation performance of the composite decreases compared to the parent CuBTC. For instance, upon the incorporation of a hydrophilic [BMIM][SCN] into the hydrophilic CuBTC, ideal CO_2/CH_4 and CO_2/N_2 selectivities of [BMIM][SCN]/CuBTC improved 1.2- and 1.6-times compared to parent CuBTC at 0.01 bar. On the other hand, when a hydrophobic [BMIM][NTf_2] was incorporated into CuBTC, gas separation performance of [BMIM][NTf_2]/CuBTC decreased compared to pristine CuBTC in the whole pressure range (0.01–1 bar). Likewise, in this work, upon the incorporation of a hydrophilic [EMIM][DEP] into CuBTC, CO_2/CH_4 and CO_2/N_2 selectivities of the IL-incorporated CuBTC improved 1.6- and 2.4-times at 0.01 bar, whereas the corresponding selectivities were improved 1.3- and 1.5-times at 0.1 bar, respectively. Here, we note that the improvement achieved in gas separation performance of [EMIM][DEP]/CuBTC composite is the highest among all of the IL/CuBTC composites.

We then compared the gas separation performance of [EMIM][DEP]/CuBTC composite with other IL/MOF composites (with different MOFs) previously reported in the literature having a comparable IL loading. Fig. 10 compares the normalized ideal CO_2/CH_4 and CO_2/N_2 selectivities of [EMIM][DEP]/CuBTC, with those of various IL/ZIF-8 and IL/MIL-53(Al) composites at 0.01 bar and 25 °C. Results showed that most of the previously reported IL/ZIF-8 and IL/MIL-53(Al) composites have a better gas separation performance compared to [EMIM][DEP]/CuBTC composite even though [EMIM][DEP]/CuBTC composite has the highest performance among all IL/CuBTC composites reported so far [25–29,57,66,67]. This difference in gas separation performance of IL/CuBTC composites compared to other IL/MOF composites was attributed to the presence of open metal sites in CuBTC, which upon the incorporation of IL interact more with anion of the IL, making them less selective for the guest molecules leading to a relatively poor gas separation performance [31]. However, we note that pristine CuBTC is one of

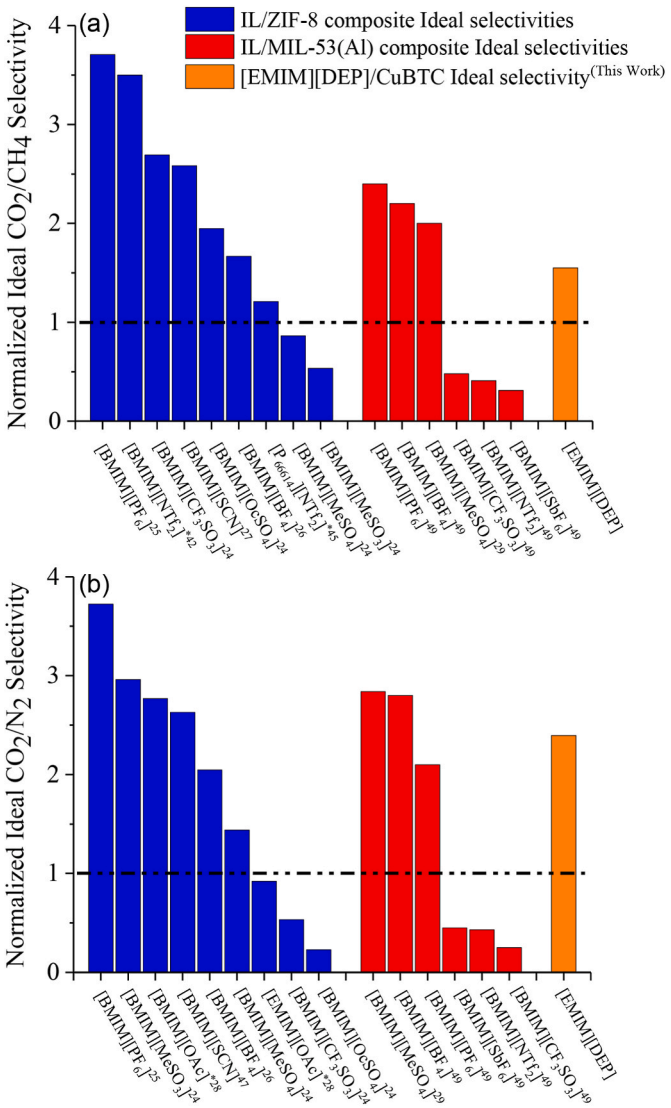

Fig. 10. Normalized ideal CO_2/CH_4 and CO_2/N_2 selectivities of [EMIM][DEP]/CuBTC, IL/ZIF-8, and IL/MIL-53(Al) composites at 0.01 bar. *Normalized selectivities were calculated from adsorption isotherm obtained at 30 °C. Ideal CO_2/CH_4 selectivities of the pristine ZIF-8 and MIL-53(Al) are 2.4 and 6.1, respectively, at 0.01 bar and the corresponding ideal CO_2/N_2 selectivities are 6.5 and 13.1, respectively, at 0.01 bar.

the few commercially available MOFs with significantly high gas adsorption capacity. Furthermore, understanding the structure-performance relations in these composites is crucial for the design and development of new composites with better CO_2 separation performance. Thus, we believe that this study will make a significant contribution to our understanding into the structure-performance relationships of the IL/CuBTC composites and provide additional insights on the structural factors controlling the IL-CuBTC interactions and their consequences on CO_2 separation performance of IL/CuBTC composites.

4. Conclusions

A new IL/MOF composite material was presented by successfully incorporating [EMIM][DEP] into CuBTC. Characterization data confirmed that the surface morphology and crystal structure of CuBTC were preserved upon the incorporation of IL. TGA and IR results exhibited the possible IL-MOF interactions, which resulted in the change of thermal stability and shifts in the IR peak positions of composite material compared to the corresponding IR features of bulk IL and pristine CuBTC. These changes in the thermal stability and the peak positions of the IR features revealed the presence of interactions occurring between the anion of the IL and the open metal sites of CuBTC. Adsorption isotherms of CO_2, CH_4, and N_2 were obtained for pristine CuBTC and IL-incorporated CuBTC. Results exhibited that upon the incorporation of IL into CuBTC, adsorption capacities of IL/CuBTC composite were lower compared to the corresponding uptakes in pristine CuBTC. However, different level of decrease in the uptake of each gas was observed, which led to improvement in the gas separation performance of CuBTC upon IL incorporation. Accordingly, at 0.01 bar, the ideal CO_2/CH_4 and CO_2/N_2 selectivities of IL/CuBTC composite improved 1.6- and 2.4-times compared to pristine CuBTC. Similarly, at 0.01 bar, CO_2/CH_4:50/50 and CO_2/N_2:15/85 separation performance of the IL-incorporated CuBTC improved 1.5- and 1.9-times than that of the corresponding selectivities of pristine CuBTC. This increase in the CO_2 separation performance of IL/CuBTC was attributed to the great affinity and better solubility of CO_2 in the IL having a phosphate-based anion compared to CH_4 and N_2.

CRediT authorship contribution statement

Muhammad Zeeshan: Conceptualization, Methodology, Validation, Formal analysis, Writing - original draft, Data curation, Investigation, Visualization, Project administration, Writing - review & editing. **Hasan Can Gulbalkan:** Methodology, Data curation. **Zeynep Pinar Haslak:** Methodology, Data curation. **Seda Keskin:** Supervision, Conceptualization, Project administration, Validation, Resources, Methodology, Writing - original draft, Data curation, Writing - review & editing. **Alper Uzun:** Supervision, Conceptualization, Project administration, Validation, Resources, Methodology, Writing - original draft, Data curation, Writing - review & editing.

Declaration of competing interest

The authors declare that they have no known competing financial interests or personal relationships that could have appeared to influence the work reported in this paper.

Acknowledgments

This work received funding from the Scientific and Technological Research Council of Turkey (TUBITAK) under 1001-Scientific and Technological Research Projects Funding Program (Project Number 114R093). This work is also supported by Koç University Seed Fund Program. S.K. acknowledges ERC-2017-Starting Grant. This study has received funding from the European Research Council (ERC) under the European Union's Horizon 2020 research and innovation programme (ERC-2017-Starting Grant, grant agreement no. 756489-COSMOS). The authors gratefully acknowledge the support of Koç University TÜPRAŞ Energy Center (KUTEM), Koç University Surface Science and Technology Center (KUYTAM), and the use of the services and facilities of Central Research Infrastructure Directorate at Koç University. The authors thank TARLA for the support in cooperative research. M.Z. acknowledges HEC Pakistan Scholarship. A.U. acknowledges the METU Mustafa Parlar Foundation of Science and Education Incentive Award.

Appendix A. Supplementary data

Supplementary data related to this article can be found at https://doi.org/10.1016/j.micromeso.2021.110947.

References

[1] D. Danaci, M. Bui, N. Mac Dowell, C. Petit, Exploring the limits of adsorption-based CO_2 capture using MOFs with PVSA-from molecular design to process economics, Mol. Syst. Des. Eng. 5 (2020) 212–231, https://doi.org/10.1039/c9me00102f.
[2] H.A. Patel, J. Byun, C.T. Yavuz, Carbon dioxide capture adsorbents: chemistry and methods, ChemSusChem 10 (2017) 1303–1317, https://doi.org/10.1002/cssc.201601545.
[3] S. Xian, J. Peng, Z. Zhang, Q. Xia, H. Wang, Z. Li, Highly enhanced and weakened adsorption properties of two MOFs by water vapor for separation of CO_2/CH_4 and CO_2/N_2 binary mixtures, Chem. Eng. J. 270 (2015) 385–392, https://doi.org/10.1016/j.cej.2015.02.041.
[4] A. Uzun, S. Keskin, Site characteristics in metal organic frameworks for gas adsorption, Prog. Surf. Sci. 89 (2014) 56–79, https://doi.org/10.1016/j.progsurf.2013.11.001.
[5] R. Atkinson, K.H. Welge, Temperature dependence of O(1S) deactivation by CO_2, O_2, N_2, and Ar, J. Chem. Phys. 57 (1972) 3689–3693, https://doi.org/10.1063/1.1678829.
[6] J. Zhang, Q. Zhang, F. Shi, S. Zhang, B. Qiao, L. Liu, Y. Ma, Y. Deng, Greatly enhanced fluorescence of dicyanamide anion based ionic liquids confined into mesoporous silica gel, Chem. Phys. Lett. 461 (2008) 229–234, https://doi.org/10.1016/j.cplett.2008.07.015.
[7] J.R. Li, R.J. Kuppler, H.C. Zhou, Selective gas adsorption and separation in metal-organic frameworks, Chem. Soc. Rev. 38 (2009) 1477–1504, https://doi.org/10.1039/b802426j.
[8] S. Chowdhury, R. Balasubramanian, Holey graphene frameworks for highly selective post-combustion carbon capture, Sci. Rep. 6 (2016) 1–10, https://doi.org/10.1038/srep21537.
[9] R. Balasubramanian, S. Chowdhury, Recent advances and progress in the development of graphene-based adsorbents for CO_2 capture, J. Mater. Chem. A. 3 (2015) 21968–21989, https://doi.org/10.1039/c5ta04822b.
[10] J. Yu, L.H. Xie, J.R. Li, Y. Ma, J.M. Seminario, P.B. Balbuena, CO_2 capture and separations using MOFs: computational and experimental studies, Chem. Rev. 117 (2017) 9674–9754, https://doi.org/10.1021/acs.chemrev.6b00626.
[11] F.P. Kinik, A. Uzun, S. Keskin, Ionic liquid/metal–organic framework composites: from synthesis to applications, ChemSusChem 10 (2017) 2842–2863, https://doi.org/10.1002/cssc.201700716.
[12] M. Zeeshan, K. Yalcin, F.E.S. Oztuna, U. Unal, S. Keskin, A. Uzun, A New Class of Porous Materials for Efficient CO_2 Separation Ionic Liquid/Graphene Aerogel Composites 171, Carbon, 2021, pp. 79–87, https://doi.org/10.1016/j.carbon.2020.08.079.
[13] I.J. Kang, N.A. Khan, E. Haque, S.H. Jhung, Chemical and thermal stability of isotypic metal-organic frameworks: effect of metal ions, Chem. Eur J. 17 (2011) 6437–6442, https://doi.org/10.1002/chem.201100316.
[14] L. Jiao, J.Y.R. Seow, W.S. Skinner, Z.U. Wang, H.L. Jiang, Metal–organic frameworks: structures and functional applications, Mater. Today 27 (2019) 43–68, https://doi.org/10.1016/j.mattod.2018.10.038.
[15] Z. Wang, S.M. Cohen, Postsynthetic modification of metal–organic frameworks, Chem. Soc. Rev. 38 (2009) 1315–1329.
[16] N. Nasirpour, M. Mohammadpourfard, S. Zeinali Heris, Ionic liquids: promising compounds for sustainable chemical processes and applications, Chem. Eng. Res. Des. 160 (2020) 264–300, https://doi.org/10.1016/j.cherd.2020.06.006.
[17] M. Hasib-ur-Rahman, M. Siaj, F. Larachi, Ionic liquids for CO_2 capture-Development and progress, Chem. Eng. Process. Process Intensif. 49 (2010) 313–322, https://doi.org/10.1016/j.cep.2010.03.008.
[18] H.M. Polat, S. Kavak, H. Kulak, A. Uzun, S. Keskin, CO_2 separation from flue gas mixture using [BMIM][BF_4]/MOF composites: linking high-throughput computational screening with experiments, Chem. Eng. J. 394 (2020) 124916, https://doi.org/10.1016/j.cej.2020.124916.
[19] K.B. Sezginel, S. Keskin, A. Uzun, Tuning the gas separation performance of CuBTC by ionic liquid incorporation, Langmuir 32 (2016) 1139–1147, https://doi.org/10.1021/acs.langmuir.5b04123.
[20] M. Zeeshan, V. Nozari, M.B. Yagci, T. Isik, U. Unal, V. Ortalan, S. Keskin, A. Uzun, Core-shell type ionic liquid/metal organic framework composite: an exceptionally high CO_2/CH_4 selectivity, J. Am. Chem. Soc. 140 (2018) 10113–10116, https://doi.org/10.1021/jacs.8b05802.

[21] N.A. Khan, Z. Hasan, S.H. Jhung, Ionic liquid@MIL-101 prepared via the ship-in-bottle technique: remarkable adsorbents for the removal of benzothiophene from liquid fuel, Chem. Commun. 52 (2016) 2561–2564, https://doi.org/10.1039/c5cc08896h.

[22] W. Xue, Z. Li, H. Huang, Q. Yang, D. Liu, Q. Xu, C. Zhong, Effects of ionic liquid dispersion in metal-organic frameworks and covalent organic frameworks on CO_2 capture: a computational study, Chem. Eng. Sci. 140 (2016) 1–9, https://doi.org/10.1016/j.ces.2015.10.003.

[23] H.M. Polat, M. Zeeshan, A. Uzun, S. Keskin, Unlocking CO_2 separation performance of ionic liquid/CuBTC composites: combining experiments with molecular simulations, Chem. Eng. J. 373 (2019) 1179–1189, https://doi.org/10.1016/j.cej.2019.05.113.

[24] M. Zeeshan, H. Kulak, S. Kavak, H.M. Polat, O. Durak, S. Keskin, A. Uzun, Influence of anion size and electronic structure on the gas separation performance of ionic liquid/ZIF-8 composites, Microporous Mesoporous Mater. 306 (2020) 110446, https://doi.org/10.1016/j.micromeso.2020.110446.

[25] F.P. Kinik, C. Altintas, V. Balci, B. Koyuturk, A. Uzun, S. Keskin, [BMIM][PF_6] incorporation doubles CO_2 selectivity of ZIF-8: elucidation of interactions and their consequences on performance, ACS Appl. Mater. Interfaces 8 (2016) 30992–31005, https://doi.org/10.1021/acsami.6b11087.

[26] B. Koyuturk, C. Altintas, F.P. Kinik, S. Keskin, A. Uzun, Improving gas separation performance of ZIF-8 by [BMIM][BF_4] incorporation: interactions and their consequences on performance, J. Phys. Chem. C 121 (2017) 10370–10381, https://doi.org/10.1021/acs.jpcc.7b00848.

[27] M. Zeeshan, S. Keskin, A. Uzun, Enhancing CO_2/CH_4 and CO_2/N_2 separation performances of ZIF-8 by post-synthesis modification with [BMIM][SCN], Polyhedron 155 (2018) 485–492, https://doi.org/10.1016/j.poly.2018.08.073.

[28] M. Mohamedali, H. Ibrahim, A. Henni, Incorporation of acetate-based ionic liquids into a zeolitic imidazolate framework (ZIF-8) as efficient sorbents for carbon dioxide capture, Chem. Eng. J. 334 (2018) 817–828, https://doi.org/10.1016/j.cej.2017.10.104.

[29] H. Kulak, H.M. Polat, S. Kavak, S. Keskin, A. Uzun, Improving CO_2 separation performance of MIL-53(Al) by incorporating 1-n-Butyl-3-Methylimidazolium methyl sulfate, Energy Technol. 7 (2019) 1900157, https://doi.org/10.1002/ente.201900157.

[30] V. Nozari, M. Zeeshan, S. Keskin, A. Uzun, Effect of methylation of ionic liquids on the gas separation performance of ionic liquid/metal-organic framework composites, CrystEngComm 20 (2018) 7137–7143, https://doi.org/10.1039/C8CE01364K.

[31] V. Nozari, S. Keskin, A. Uzun, Toward rational design of ionic liquid/metal-organic framework composites: effects of interionic interaction energy, ACS Omega 2 (2017) 6613–6618, https://doi.org/10.1021/acsomega.7b01074.

[32] M. Mohamedali, A. Henni, H. Ibrahim, Markedly improved CO_2 uptake using imidazolium-based ionic liquids confined into HKUST-1 frameworks, Microporous Mesoporous Mater. 284 (2019) 98–110, https://doi.org/10.1016/j.micromeso.2019.04.004.

[33] J.M. Vicent-Luna, J.J. Gutiérrez-Sevillano, J.A. Anta, S. Calero, Effect of room-temperature ionic liquids on CO_2 separation by a Cu-BTC metal-organic framework, J. Phys. Chem. C 117 (2013) 20762–20768, https://doi.org/10.1021/jp407176j.

[34] M. Zeeshan, V. Nozari, S. Keskin, A. Uzun, Structural factors determining thermal stability limits of ionic liquid/MOF composites: imidazolium ionic liquids combined with CuBTC and ZIF-8, Ind. Eng. Chem. Res. 58 (2019) 14124–14138, https://doi.org/10.1021/acs.iecr.9b02415.

[35] J. Wang, C. Petit, X. Zhang, A.H.A. Park, Simultaneous measurement of CO_2 sorption and swelling of phosphate-based ionic liquid, Green Energy Environ. 1 (2016) 258–265, https://doi.org/10.1016/j.gee.2016.11.004.

[36] A. Zicmanis, S. Zeltkalne, Ionic liquids with dimethyl phosphate anion as highly efficient materials for technological processes: a review, Int. J. Petrochem. Res. 2 (2018) 116–125, https://doi.org/10.18689/ijpr-1000121.

[37] M. Wojdyr, Fityk: a general-purpose peak fitting program, J. Appl. Crystallogr. 43 (2010) 1126–1128, https://doi.org/10.1107/S0021889810030499.

[38] S. Lee, J.H. Lee, J. Kim, User-friendly graphical user interface software for ideal adsorbed solution theory calculations, Kor. J. Chem. Eng. 35 (2018) 214–221, https://doi.org/10.1007/s11814-017-0269-9.

[39] D. Dubbeldam, S. Calero, D.E. Ellis, R.Q. Snurr, RASPA: molecular simulation software for adsorption and diffusion in flexible nanoporous materials, Mol. Simulat. 42 (2016) 81–101, https://doi.org/10.1080/08927022.2015.1010082.

[40] S.L. Mayo, B.D. Olafson, W.A. Goddard, DREIDING: a generic force field for molecular simulations, J. Phys. Chem. 94 (1990) 8897–8909, https://doi.org/10.1021/j100389a010.

[41] J.J. Potoff, J.I. Siepmann, Vapor–liquid equilibria of mixtures containing alkanes, carbon dioxide, and nitrogen, AIChE J. 47 (2001) 1676–1682.

[42] D. Dubbeldam, S. Calero, T.J.H. Vlugt, R. Krishna, T.L.M. Maesen, B. Smit, United atom force field for alkanes in nanoporous materials, J. Phys. Chem. B 108 (2004) 12301–12313, https://doi.org/10.1021/jp0376727.

[43] K. Makrodimitris, G.K. Papadopoulos, D.N. Theodorou, Prediction of permeation properties of CO_2 and N_2 through silicalite via molecular simulations, J. Phys. Chem. B 105 (2001) 777–788.

[44] C.E. Wilmer, R.Q. Snurr, Towards rapid computational screening of metal-organic frameworks for carbon dioxide capture: calculation of framework charges via charge equilibration, Chem. Eng. J. 171 (2011) 775–781, https://doi.org/10.1016/j.cej.2010.10.035.

[45] A.D. Becke, Density-functional thermochemistry. I. The effect of the exchange-only gradient correction, J. Chem. Phys. 96 (1992) 2155–2160, https://doi.org/10.1063/1.462066.

[46] C. Lee, W. Yang, R.G. Parr, Development of the Colle-Salvetti correlation-energy formula into a functional of the electron density, Phys. Rev. B 37 (1988) 785–789, https://doi.org/10.1103/PhysRevB.37.785.

[47] S. Grimme, J. Antony, S. Ehrlich, H. Krieg, A consistent and accurate ab initio parametrization of density functional dispersion correction (DFT-D) for the 94 elements H-Pu, J. Chem. Phys. 132 (2010) 154104.

[48] R. Anantharaj, T. Banerjee, COSMO-RS-based screening of ionic liquids as green solvents in denitrification studies, Ind. Eng. Chem. Res. 49 (2010) 8705–8725, https://doi.org/10.1021/ie901341k.

[49] C. Hardacre, J. Jacquemin, N. Ab Manan, D.W. Rooney, T.G.A. Youngs, Prediction of gas solubility using COSMOthermX, ACS Symp. Ser. 1030 (2009) 359–383, https://doi.org/10.1021/bk-2009-1030.ch024.

[50] Y.S. Sistla, A. Khanna, Validation and prediction of the temperature-dependent Henry's constant for CO_2-ionic liquid systems using the Conductor-like Screening Model for Realistic Solvation (COSMO-RS), J. Chem. Eng. Data 56 (2011) 4045–4060, https://doi.org/10.1021/je200486c.

[51] R. Hernández-Bravo, A.D. Miranda, O. Martínez-Mora, Z. Domínguez, J. M. Martínez-Magadán, R. García-Chávez, J.M. Domínguez-Esquivel, Calculation of the solubility parameter by COSMO-RS methods and its influence on asphaltene-ionic liquid interactions, Ind. Eng. Chem. Res. 56 (2017) 5107–5115, https://doi.org/10.1021/acs.iecr.6b05035.

[52] L. Wang, F. Zhang, C. Wang, Y. Li, J. Yang, L. Li, J. Li, Ethylenediamine-functionalized metal organic frameworks MIL-100(Cr) for efficient CO_2/N_2O separation, Separ. Purif. Technol. 235 (2020) 116219, https://doi.org/10.1016/j.seppur.2019.116219.

[53] B. Van Der Bruggen, J. Schaep, D. Wilms, C. Vandecasteele, Influence of molecular size, polarity and charge on the retention of organic molecules by nanofiltration, J. Membr. Sci. 156 (1999) 29–41, https://doi.org/10.1016/S0376-7388(98)00326-3.

[54] A. Vishnyakov, P.I. Ravikovitch, A.V. Neimark, M. Bülow, Q.M. Wang, Nanopore structure and sorption properties of Cu-BTC metal-organic framework, Nano Lett. 3 (2003) 713–718, https://doi.org/10.1021/nl0341281.

[55] M.M. Peng, D.K. Kim, A. Aziz, K.R. Back, U.J. Jeon, H.T. Jang, CO_2 adsorption of metal organic framework material Cu-BTC via different preparation routes. Commun. Comput. Inf. Sci., Springer, 2012, pp. 244–251, https://doi.org/10.1007/978-3-642-35248-5-34.

[56] R. Mahugo, A. Mayoral, M. Sánchez-Sánchez, I. Diaz, Observation of Ag nanoparticles in/on Ag@MIL-100(Fe) prepared through different procedures, Front. Chem. 7 (2019) 686, https://doi.org/10.3389/fchem.2019.00686.

[57] Y. Ban, Z. Li, Y. Li, Y. Peng, H. Jin, W. Jiao, A. Guo, P. Wang, Q. Yang, C. Zhong, W. Yang, Confinement of ionic liquids in nanocages: tailoring the molecular sieving properties of ZIF-8 for membrane-based CO_2 capture, Angew. Chem. Int. Ed. 54 (2015) 15483–15487, https://doi.org/10.1002/anie.201505508.

[58] H. Liu, S. Chen, X. Li, R. Zhao, Y. Sun, Preparation of [EMIM]DEP/$2C_3H_4O_4$ DESs and its oxidative desulfurization performance, Separ. Sci. Technol. (2020) 1–9, https://doi.org/10.1080/01496395.2020.1717532.

[59] S. Dubey, P. Bharmoria, P.S. Gehlot, V. Agrawal, A. Kumar, S. Mishra, 1-Ethyl-3-methylimidazolium diethylphosphate based extraction of bioplastic "polyhydroxyalkanoates" from bacteria: green and sustainable approach, ACS Sustain. Chem. Eng. 6 (2018) 766–773, https://doi.org/10.1021/acssuschemeng.7b03096.

[60] E. Akar, Y. Seki, O. Özdemir, I. Şen, M. Sarikanat, B.O. Gürses, Ö.C. Yilmaz, L. Çetin, K. Sever, Electromechanical characterization of multilayer graphene-reinforced cellulose composite containing 1-ethyl-3-methylimidazolium diethylphosphonate ionic liquid, Sci. Eng. Compos. Mater. 24 (2017) 289–295, https://doi.org/10.1515/secm-2015-0038.

[61] M. Li, Y. Li, W. Li, F. Liu, X. Qi, M. Xue, Y. Wang, C. Zhao, Synthesis and application of Cu-BTC@ZSM-5 composites as effective adsorbents for removal of toluene gas under moist ambience: kinetics, thermodynamics, and mechanism studies, Environ. Sci. Pollut. Res. 27 (2020) 6052–6065, https://doi.org/10.1007/s11356-019-07293-2.

[62] J. Cheng, X. Xuan, X. Yang, J. Zhou, K. Cen, Preparation of a Cu(BTC)-rGO catalyst loaded on a Pt deposited Cu foam cathode to reduce CO_2 in a photoelectrochemical cell, RSC Adv. 8 (2018) 32296–32303, https://doi.org/10.1039/c8ra05964k.

[63] D. Tuncel, A.N. Ökte, Efficient photoactivity of TiO_2 -hybrid-porous nanocomposite: effect of humidity, Appl. Surf. Sci. 458 (2018) 546–554, https://doi.org/10.1016/j.apsusc.2018.07.130.

[64] A. Indarto, J. Palgunadi, Prediction of binding bond energy between phosphorous-based ionic liquids and CO_2. Assessment of the CO_2-anion interactions, Ionics (Kiel). 18 (2012) 143–150, https://doi.org/10.1007/s11581-011-0606-7.

[65] C.M. Simon, B. Smit, M. Haranczyk, PyIAST: ideal adsorbed solution theory (IAST) Python package, Comput. Phys. Commun. 200 (2016) 364–380, https://doi.org/10.1016/j.cpc.2015.11.016.

[66] S. Kavak, H.M. Polat, H. Kulak, S. Keskin, A. Uzun, MIL-53(Al) as a versatile platform for ionic-liquid/MOF composites to enhance CO_2 selectivity over CH_4 and N_2, Chem. Asian J. 14 (2019) 3655–3667, https://doi.org/10.1002/asia.201900634.

[67] T.J. Ferreira, R.P.P.L. Ribeiro, J.P.B. Mota, L.P.N. Rebelo, J.M.S.S. Esperança, I.A. A.C. Esteves, Ionic liquid-impregnated metal-organic frameworks for CO_2/CH_4 separation, ACS Appl. Nano Mater. 2 (2019) 7933–7950, https://doi.org/10.1021/acsanm.9b01936.